

SELF-SHADOWING EFFECTS OF SLIM ACCRETION DISKS IN ACTIVE GALACTIC NUCLEI:
DIVERSE APPEARANCE OF THE BROAD-LINE REGIONJIAN-MIN WANG^{1,2}, JIE QIU¹, PU DU¹, AND LUIS C. HO^{3,4}*Received 2014 May 11; accepted 2014 October 18*

ABSTRACT

Supermassive black holes in active galactic nuclei (AGNs) undergo a wide range of accretion rates, which lead to diversity of appearance. We consider the effects of anisotropic radiation from accretion disks on the broad-line region (BLR), from the Shakura-Sunyaev regime to slim disks with super-Eddington accretion rates. The geometrically thick funnel of the inner region of slim disks produces strong self-shadowing effects that lead to very strong anisotropy of the radiation field. We demonstrate that the degree of anisotropy of the radiation fields grows with increasing accretion rate. As a result of this anisotropy, BLR clouds receive different spectral energy distributions depending on their location relative to the disk, resulting in diverse observational appearance of the BLR. We show that the self-shadowing of the inner parts of the disk naturally produces two dynamically distinct regions of the BLR, depending on accretion rate. These two regions manifest themselves as kinematically distinct components of the broad H β line profile with different line widths and fluxes, which jointly account for the Lorentzian profile generally observed in narrow-line Seyfert 1 galaxies. In the time domain, these two components are expected reverberate with different time lags with respect to the varying ionizing continuum, depending on the accretion rate and the viewing angle of the observer. The diverse appearance of the BLR due to the anisotropic ionizing energy source can be tested by reverberation mapping of H β and other broad emission lines (e.g., Fe II), providing a new tool to diagnose the structure and dynamics of the BLR. Other observational consequences of our model are also explored.

Subject headings: galaxies: active – accretion, accretion disk

1. INTRODUCTION

Broad Balmer emission lines in active galactic nuclei (AGNs) are main features of their optical spectra. As originally suggested by Woltjer (1959), the large widths of the emission lines are generally thought to arise from virial motions of clouds orbiting around a central supermassive black hole (Rees 1984; Osterbrock & Mathews 1986). It has been established that the broad emission lines arise from clouds in the broad-line region (BLR) photoionized by a central continuum source produced by an accretion disk around the central black hole (Rees 1984; Ho 2008; Netzer 2013). The smooth profiles of AGN spectra suggest that the number of clouds is large (Arav et al. 1997, 1998). Reverberation mapping of ~ 50 AGNs has revealed that the size of the BLR, as measured for H β , correlates well with the continuum luminosity (Kaspi et al. 2000); the latest study of Bentz et al. (2013) reports $R_{\text{H}\beta} \approx 33 L_{44}^{0.53} \text{ltd}$, where $R_{\text{H}\beta}$ is the distance of the H β -emitting regions from the center and L_{44} is the continuum luminosity at 5100 Å in unit of $10^{44} \text{erg s}^{-1}$. Defining the ionisation parameter as $U = Q_{\text{ion}}/4\pi R_{\text{H}\beta}^2 c n_e$, where n_e is the electron density of the clouds, Q_{ion} is the rate of ionizing photons, and c is the speed of light, this empirical $R_{\text{BLR}} - L$ relation can be explained by photoionized BLR clouds that roughly have constant $n_e U$ (e.g., Wandel et al. 1999; Bentz et al. 2013). Here $Q_{\text{ion}} (\propto L_{\text{ion}}$, the ionising luminosity) is

proportional to L_{5100} for a canonical spectral energy distribution (SED). This relation assumes that all clouds in the BLR and the observer at infinity see the same SED of the ionizing source. However, we still poorly understand the geometry and dynamics of the BLR. Only a limited sample of AGNs has been studied with reverberation mapping, and the intrinsic scatter of the $R_{\text{H}\beta} - L_{5100}$ relation is poorly unknown. The BLR of AGNs shows very diverse spectral properties (e.g., Boroson & Green 1992; Shen & Ho 2014). This leads Peterson (2006) to ask: “Where does the energy to power the emission lines come from? The BLR energy budget problem is still unsolved. The observed AGN continuum is neither luminous enough nor hard enough to account for the broad lines. Does the BLR see a different continuum than we do, or is there an energy source we have not yet recognized?”

From a theoretical perspective, AGNs with very high accretion rates may offer a promising avenue to addressing some of these longstanding problems. Accretion disks become geometrically thick with increasing accretion rates so that self-shadowing effects are important, leading to strongly anisotropic illumination of the BLR. AGNs with accretion rates in the Shakura & Sunyaev (1973, hereafter SS) regime have been extensively studied. Netzer (1987) discusses the effects of anisotropic emissions from geometrically thin disks on emission lines; he treats limb darkening and the $\cos\theta(1 + 2\cos\theta)$ angular dependence of the radiation intensity, where θ is the angle of line of sight to the disk axis. Although the radiation from geometrically thin disks shows anisotropy through the $\cos\theta$ term, the observational consequences on the BLR are minimal. By contrast, accretion flows with high accretion rates, known as slim disks (Abramowicz et al. 1988), develop sharp funnels as a consequence of their geometrically thick structure when they have accretion rates higher than a few L_{Edd}/c^2 , where L_{Edd} is the Eddington luminosity. This

¹ Key Laboratory for Particle Astrophysics, Institute of High Energy Physics, Chinese Academy of Sciences, 19B Yuquan Road, Beijing 100049, China.

² National Astronomical Observatories of China, Chinese Academy of Sciences, 20A Datun Road, Beijing 100020, China

³ Kavli Institute for Astronomy and Astrophysics, Peking University, Beijing 100875, China

⁴ Department of Astronomy, School of Physics, Peking University, Beijing 100875, China

is expected to produce much more dramatic anisotropic illumination of the BLR. In the nearby Universe, slim disks are believed to power narrow-line Seyfert 1 galaxies (NLS1; Osterbrock & Pogge 1985), which contain relatively low-mass black holes with higher accretion rates (Boller et al. 1996; Wang & Netzer 2003). Direct observational evidence for slim disks is still relatively scarce (but see Kawaguchi et al. 2004; Desroches et al. 2009; Jin et al. 2009), limited by the availability of reliable SED predictions for this regime of accretion rates. Some effects of the anisotropic radiation on SEDs have been discussed by Czerny & Elvis (1987) for standard disks with higher accretion rates and Madau (1988) for simplified tori. Watarai et al. (2005) and Li et al. (2010) studied the geometric effects of slim disks on SEDs of ultraluminous X-ray sources. However, the effects of anisotropic illumination of a slim disk on the BLR of AGNs have not been explored in the published literature. This is the subject of our current work.

Beginning with a general treatment of the structure of accretion disks from low to high accretion rates, we show that the self-shadowing effects of the funnel in a slim disk produce a strong angular dependence of the radiation field. The high degree of anisotropy of the radiation field naturally defines two spatially and kinematically distinct regions in the BLR. §2 is devoted to the details of the anisotropic radiation field. §3 elucidates the two-component nature of the H β -emitting region and relevant consequences of the BLR in the time domain. Observational implications beyond the BLR are discussed in §4. The last section presents a brief summary.

2. ANISOTROPIC RADIATION OF SLIM ACCRETION DISKS

2.1. Slim Disks

The geometry of accretion disks, which is controlled by the accretion mode, determines the anisotropy of the radiation field. The accretion mode is governed by the dimensionless accretion rate, defined by

$$\dot{\mathcal{M}} = \frac{\dot{M}_\bullet}{L_{\text{Edd}} c^2}, \quad (1)$$

where \dot{M}_\bullet is the accretion rate, the Eddington luminosity $L_{\text{Edd}} = 4\pi GM_\bullet cm_p/\sigma_T$, M_\bullet is the black hole mass, G is the gravitational constant, m_p is the proton mass, and σ_T is the Thomson cross section. SS disks in the sub-Eddington regime ($\dot{\mathcal{M}} \lesssim 1$) are characterized by the following features (see Frank et al. 2002): (1) Keplerian angular momentum distribution; (2) energy balance between dissipation and radiative cooling is localized so that radial advection of energy can be neglected; and (3) the disk maintains a geometrically thin configuration. The anisotropy of an SS disk simply depends on the factor $\cos\theta(1+2\cos\theta)$ because the disk is geometrically thin. It should be noted that most AGNs studied with reverberation mapping (Bentz et al. 2013) are in the SS regime. The anisotropy of SS disks is much weaker than that of slim disks.

When the accretion rate $\dot{\mathcal{M}}$ increases, the above-mentioned features dramatically change. In such a situation, the angular momentum distribution is sub-Keplerian, the radial velocity of the accretion flow becomes comparable with the Keplerian rotation, which leads to strong photon trapping and a saturated luminosity, and, in particular, the inner parts of the disk develop a sharp funnel. The funnel produces strong self-shadowing effects depending on the actual accretion rates. There has been increasing attention on numerical simulations of slim disks (Ohsuga et al. 2005; McKinney et al. 2014;

Sadowski et al. 2014; Yang et al. 2014; Jiang et al. 2014). The general properties of slim disks from these simulations agree with the solutions derived from the vertically averaged equations of the disk.

For explicit discussion of the effect of slim disks on the BLR, we start from the averaged equations for slim disks. Hoshi (1977) introduced the polytropic relation $p = k_0 \rho^{1+1/N}$, where N is the polytropic index and k_0 is a constant, and vertically integrated the equations for an axisymmetric accretion disk. For convenience to the readers, we give the vertically averaged equations of slim disks (e.g., Muchotrzeb & Paczynski 1982; Matsumoto et al. 1984; Abramowicz et al. 1988; Watarai et al. 2005). In this paper, we use the pseudo-Newtonian potential given by $\Phi = -GM_\bullet/(R - 2r_g)$, where $R = (r^2 + z^2)^{1/2}$ and $r_g = GM_\bullet/c^2$ is the Schwarzschild radius.

2.1.1. Equations of Slim Disks

The mass conservation of a stationary slim disk reads

$$\dot{M}_\bullet = -2\pi r \Sigma v_r, \quad (2)$$

where v_r is the radial velocity of the accreting gas, $\Sigma = 2I_N H \rho$ is the surface density, $I_N = (2^N N!)^2 / (2N + 1)!$ is the average coefficient and ρ is density. Angular momentum conservation is governed by

$$\dot{M}_\bullet (\ell - \ell_{\text{in}}) = -2\pi r^2 T_{r\phi}, \quad (3)$$

where ℓ and ℓ_{in} are the specific angular momentum at r and at the inner edge r_{in} , and $T_{r\phi}$ is the turbulent viscosity. The radial motion follows from

$$v_r \frac{dv_r}{dr} + \frac{1}{\Sigma} \frac{d\Pi}{dr} = \frac{\ell^2 - \ell_K^2}{r^3} - \frac{\Pi}{\Sigma} \frac{d \ln \Omega_K}{dr}, \quad (4)$$

where $\Pi = \int p dz = 2I_{N+1} p H$ is the integrated pressure, p is the total pressure, $\Omega_K = (GM_\bullet/r)^{1/2}/(r - 2r_g)$ is the Keplerian rotation velocity and $\ell_K = r^2 \Omega_K$ is the Keplerian angular momentum. We adopt the α prescription for the viscosity (SS), such that $T_{r\phi} = -\alpha \Pi$. The vertical structure maintains a static equilibrium

$$H^2 = \frac{2(N+1)I_N}{I_{N+1}} \frac{\Pi}{\Omega_K^2 \Sigma}, \quad (5)$$

where H is the height of the disk. We use $N = 3$ in our calculations. The non-local energy budget is given by

$$Q_{\text{dis}} = Q_{\text{adv}} + Q_{\text{rad}}, \quad (6)$$

where Q_{dis} is the rate through which viscosity dissipates the gravitational energy of the accretion flow, Q_{adv} is the advection rate, and Q_{rad} is the radiative flux from the surface of the disk. The dissipation rate is given by

$$Q_{\text{dis}} = r T_{r\phi} \frac{d\Omega}{dr}. \quad (7)$$

According to the thermal dynamics of the gas, the advection rate is

$$Q_{\text{adv}} = \frac{9}{16\pi r} \dot{M}_\bullet T \left(\frac{dS}{dr} \right), \quad (8)$$

where the entropy is given by $dS = [(12 - 10.5\beta)d\ln T - (4 - 3\beta)d\ln \rho]$, $\beta = p_{\text{gas}}/(p_{\text{gas}} + p_{\text{rad}})$ is the fraction of the gas pressure relative to the total pressure, $p_{\text{rad}} = aT^4/3$ is the radiation pressure, and a is the blackbody

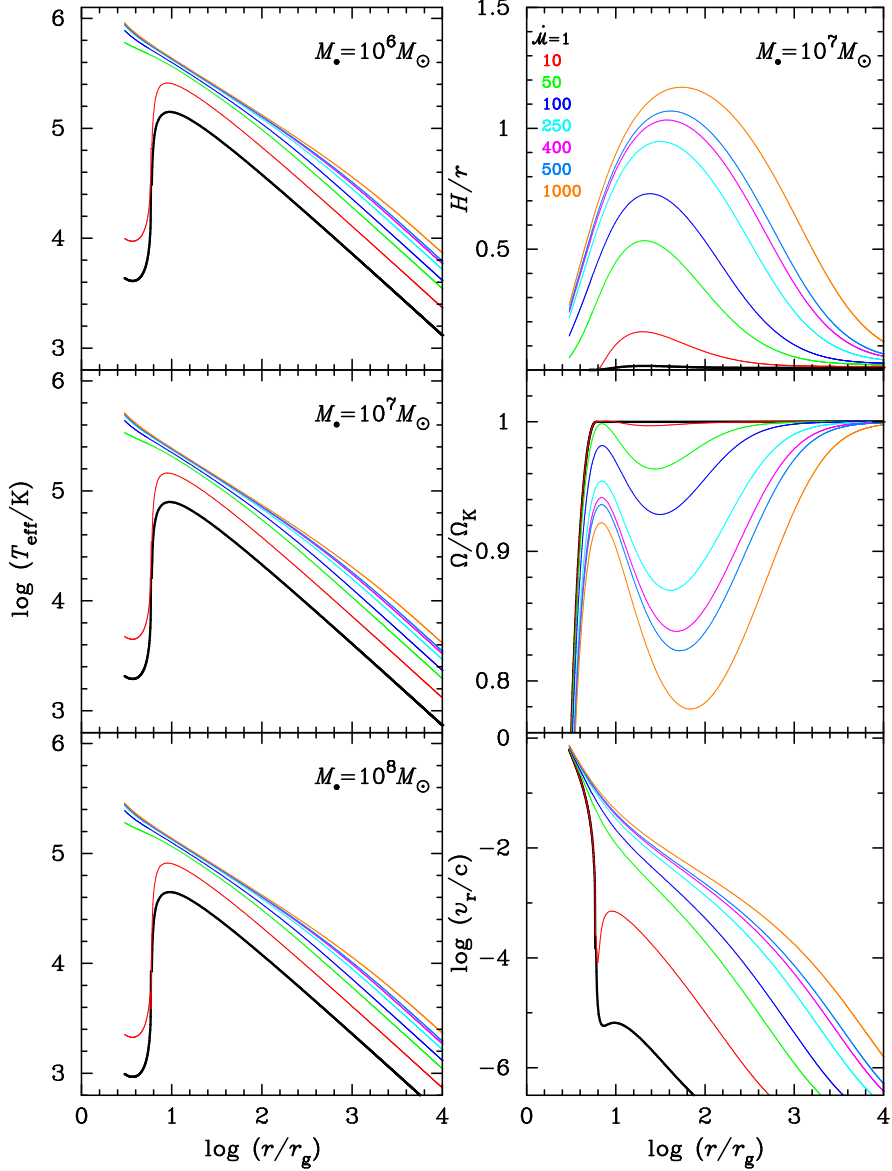


FIG. 1.— Structure of slim disks for given black hole masses and accretion rates (labeled by lines of different color). The panels on the left column plot the radial variation of effective temperature for $M_{\bullet} = 10^6, 10^7, 10^8 M_{\odot}$. The panels on the right column plot the radial variation of H/r , Ω/Ω_K , and v_r/c only for $M_{\bullet} = 10^7 M_{\odot}$, as these quantities are rather insensitive to M_{\bullet} . Slim disks are characterized by (1) $H/r \sim 1$, (2) effective temperature $T_{\text{eff}} \propto r^{-1/2}$ and decreases with black hole mass, (3) sub-Keplerian rotation, and (4) transonic accretion flows. These properties differ from those of Shakura-Sunyaev disks.

radiation constant. Using the diffusion approximation, the cooling rate can be written as

$$\mathcal{Q}_{\text{rad}} = \frac{8}{3} \frac{a c T^4}{\tau}, \quad (9)$$

where $\tau = (\kappa_{\text{es}} + \bar{\kappa}_{\text{ff}}) \Sigma$ is the optical depth. Here $\kappa_{\text{es}} = 0.34$ is the opacity of electron scattering and the Rossland mean opacity $\bar{\kappa}_{\text{ff}} = 6.5 \times 10^{22} \rho T^{-3.5}$. The diffusion approximation holds well for high accretion rates.

2.1.2. Structure and Radiation

The detailed structure of slim disks has been presented by Abramowicz et al. (1988), Watarai et al. (2005), and Li et al. (2010) for stellar mass black holes and by Szuszkiewicz et al. (1996), Mineshige et al. (2000), and Chen & Wang (2004) for supermassive black holes. Here we calculate the

structure of slim disks to study their self-shadowing effects for supermassive black holes spanning a large range of accretion rates.

Figure 1 shows the disk structure for different black hole masses and accretion rates. For SS disks, we still get transonic structures, which allow us to avoid the density singularity at the inner edge. The disks are generally geometrically thin, namely, $h \lesssim 10^{-2}$, where $h = H/r$, even in the radiation pressure-dominated regions, have Keplerian angular momentum distributions, and effective temperature distribution of $T_{\text{eff}} \propto r^{-3/4}$. Compared with geometrically thin disks, slim disks have the following main dynamical features: (1) $h \sim 1$ for $r < 10^3 r_g$, reaching $h \sim 10^{-2}$ in the outer regions; (2) the effective temperature $T_{\text{eff}} \propto r^{-1/2}$, which is different

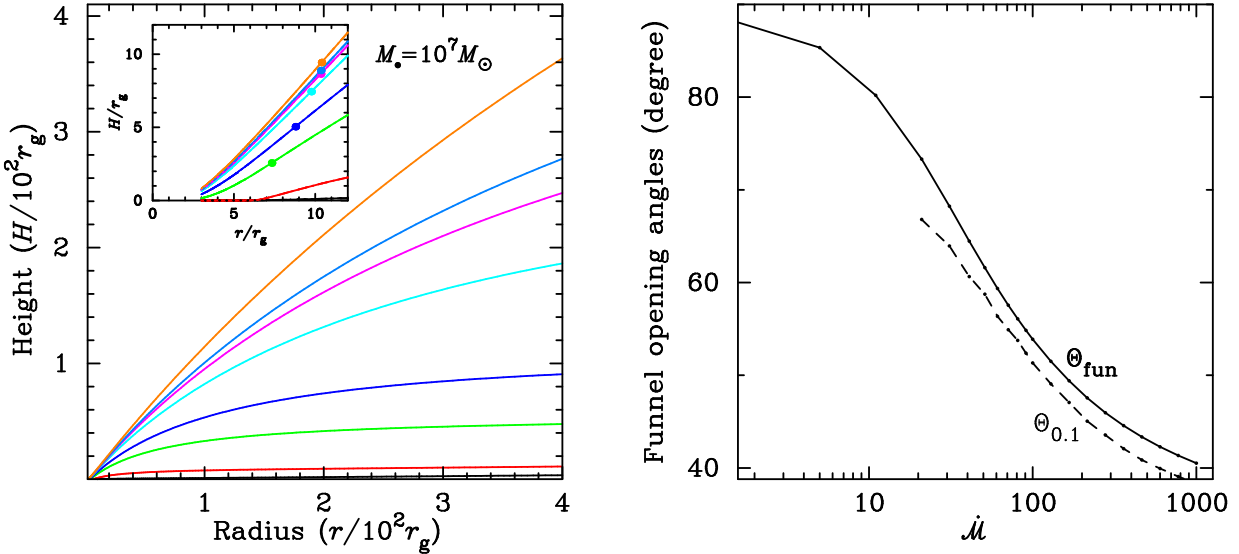


FIG. 2.— (Left) The variation of the height of slim accretion disks with different parameters. We assume a viscosity parameter $\alpha = 0.1$ and $M_{\bullet} = 10^7 M_{\odot}$. The values of black hole mass and accretion rate are labeled. Slim disks show funnels. In the inserted panel, the points on the curves mark the radius ($r_{0.1}$) obtained from Wien's law with a temperature of 0.1 keV. For a given accretion rate, the shape of a slim disk is very insensitive to black hole mass, but it depends strongly on \dot{M} for a given black hole mass. (Right) Variation of the half opening angle of the funnel (Θ_{fun}) as a function of \dot{M} ; here we use $M_{\bullet} = 10^7 M_{\odot}$. We find that the shape of the disk at radius $r_{0.1} \Theta_{0.1} \lesssim \Theta_{\text{fun}}$ with very little dependence on black hole mass.

from $T_{\text{eff}} \propto r^{-3/4}$ in geometrically thin disks; (3) radial velocity of the accretion flow is transonic, $v_r \sim v_{\text{K}}$, where v_{K} is the Keplerian rotation velocity, leading to fast transportation of radiation into the black hole through photon trapping; (4) rotation of the accretion flow is sub-Keplerian. These properties are generally consistent with Abramowicz et al. (1988), Szuszkiewicz et al. (1996), Chen & Wang (2004), and Watarai et al. (2005). These dynamical behaviors lead to radiation properties that differ from those in a SS disk.

The fast radial transportation of accretion flows leads to inefficient radiation from the disk surface caused by very large optical depth to Thomson scattering. This crucial property has two consequences. First, as a result of the effective temperature dependence of $T_{\text{eff}} \propto r^{-1/2}$, the emergent spectrum is characterized by $F_{\nu} \propto \nu^{-1}$. And second, the radiative efficiency $\eta \propto \dot{M}^{-1}$, such that the luminosity saturates as

$$L_{\bullet} \approx 2L_{\text{Edd}} \left[1 + \ln \left(\dot{M}/50 \right) \right]. \quad (10)$$

This approximation derives from a fit to numerical results (Mineshige et al. 2000) and is consistent with the self-similar solution for slim disks (Wang & Zhou 1999). The saturated luminosity is only logarithmically dependent on accretion rate and is linearly proportional to black hole mass. This unique property of slim disks suggests that super-Eddington accreting massive black holes (SEAMBHs) potentially may serve as standard candles for cosmology, provided that black hole masses can be measured accurately by reverberation mapping (Wang et al. 2013). A recent AGN reverberation mapping campaign shows that SEAMBHs are a promising new tool for cosmology of the high- z Universe (Du et al. 2014; Wang et al. 2014).

In our simplified model of slim disks, the saturated luminosity still depends on $\ln \dot{M}$. For more accurate application of SEAMBHs as standard candles for precision cosmology, it is still important for us to try to constrain \dot{M} . Although the emergent spectra is highly insensitive to the accretion rate,

fortunately, the *shape* of the slim disk itself *is* sensitive to \dot{M} once accretion rates are sufficiently high. As we discuss below, self-shadowing effects arising from the geometric shape of the slim disk strongly influence the illumination of the BLR. This gives an opportunity to constrain the accretion rate from observations of the BLR emission.

2.2. Geometry and Anisotropic Radiation

2.2.1. Funnel in Slim Disks

We obtain solutions for the structure of accretion disks from sub-Eddington accretion rates to extremely high, super-Eddington rates ($\dot{M} \gg 1$). This allows us to build up the smooth transition from SS to slim disks. The general features of the disk geometry are characterized by the appearance of sharper funnels with increasing \dot{M} . The first row of panels in Figure 1 shows the relative height of the disk for different values of M_{\bullet} and \dot{M} . We find that h is very insensitive to the black hole mass. The shape of a slim disk has three notable features: (1) a funnel develops in the innermost region [$dh/dr > 0$]; (2) a flattened part [$dh/dr < 0$ and $h \sim 1$]; (3) and a geometrically thin part ($h \sim 10^{-2}$), approaching the SS regime, in which the funnel disappears.

The left panel of Figure 2 shows the height of the disk as a function of radius; the funnel structure is clearly evident. The height of the funnel increases with accretion rates. There is a critical point, which can be used to define the funnel radius (r_{fun}), wherein h reaches its maximum value [$dh/dr = 0$]; we denote the disk height H_{fun} at r_{fun} . We define $\Theta_{\text{fun}} = \arctan(r_{\text{fun}}/H_{\text{fun}})$ as the half angle of the funnel. From the numerical results in Figure 1, we approximate $r_{\text{fun}}/r_g \approx 24\dot{M}_{100}^{0.38}$, where $\dot{M}_{100} = \dot{M}/100$. We note that the photon-trapping radius can be approximated by $r_{\text{ph}}/r_g \approx 50(\dot{M}/50)$ (Equation 22 in Wang & Zhou 1999), which is larger than r_{fun} and much more sensitive to accretion rate. This guarantees that photon-trapping processes dominate in the funnel region

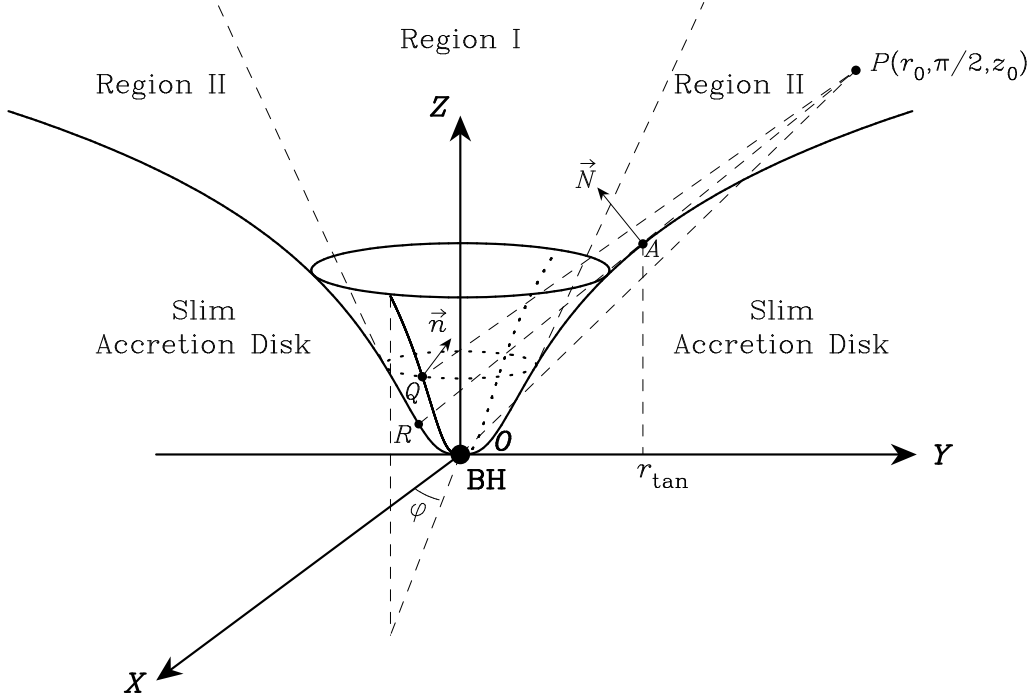


FIG. 3.— Cross section of the system along the z -axis of symmetry, including the accretion disk and the BLR. The mid plane of the disk is in the XOY plane with the origin centered on the black hole. The funnel of the slim disk divides the BLR into two regions: Region I is illuminated by the entire disk and Region II is illuminated by part of the disk. The point $P(r_0, \pi/2, z_0)$ in the BLR has the tangent line AP at point A on the surface of the disk and cross point R at the surface of the disk. The direction vector of the cloud is \vec{n}_0 , and the vector normal to line QP is \vec{n}_1 .

and that the BLR size is mainly determined by the saturated luminosity.

We digress for a moment to point out the radiation distribution along with accretion disks. Since the surface flux $F \propto x^{-3} [1 - (x_{\text{in}}/x)^{1/2}]$, the fraction of the dissipated energy within x is given by $f(x) = 1 - 3x_{\text{in}}x^{-1} + 2(x_{\text{in}}x^{-1})^{3/2}$, where $x = r/r_g$ and x_{in} is the inner edge of the disk. For a Schwarzschild black hole, $x_{\text{in}} = 6$, and we have $f(x) = (0.5, 0.8)$ for $x \approx (24, 73)$, namely that most of the gravitational energy is released within a few tens of Schwarzschild radii. Although its formation mechanism remains uncertain, the corona is expected to follow the distribution of gravitational energy release (e.g., Svensson & Zdziarski 1994; Merloni & Fabian 2002; Wang et al. 2004; Uzdensky 2013). The corona itself may be less anisotropic than the disk, but it should still be shadowed to the BLR clouds by the slim disk. And while the corona generates hard X-rays, the fraction of gravitational energy dissipated in the hot corona decreases with increasing accretion rate, generally limited to less than $\sim 15\%$ in NLS1s (Wang et al. 2004; Yang et al. 2007; see Table 6 in Grupe et al. 2010). Therefore, hard X-rays play only a minor role in powering H β emission, compared to UV and soft X-rays, which come from the innermost regions of the slim disk. As we show below, strong soft X-ray emission is one of the characteristics of slim disks, and the UV and soft X-rays are highly anisotropic with respect to the BLR clouds.

The portion of the ionizing source that reaches the BLR is determined by the relative orientation between the clouds and the surface of the disk. For H β line emission, we define the radius of the disk with a temperature of ~ 0.1 keV (the main drivers of H β emissions) as $r_{0.1}$. We find $r_{0.1}/r_g \approx 8.0\dot{M}_{100}^{0.18}$. If the $r \lesssim r_{0.1}$ regions are partially obscured by

self-shadowing, the region with ionized hydrogen atoms will shrink. It is thus useful to define the opening angle of the funnel for the H β -emitting region by the shape of the disk at radius $r_{0.1}$. The right panel of Figure 2 shows that Θ_{fun} and $\Theta_{0.1}$ are approximately equal to each other. Consequently, the opening angle of the funnel can be determined by the tangent direction at $r_{0.1}$:

$$\Theta_{0.1} = \arctan(H_r^{-1})_{0.1} \approx \begin{cases} 60^\circ - 33^\circ \log(\dot{M}/50) & (\text{for } 10 \lesssim \dot{M} \lesssim 100), \\ 52^\circ - 12^\circ \log(\dot{M}/100) & (\text{for } \dot{M} \gtrsim 100), \end{cases} \quad (11)$$

where $H_r = dH/dr$ and the subscript 0.1 is H_r at $r_{0.1}$. The opening angle decreases faster for lower accretion rates ($\dot{M} \lesssim 100$), while it changes slower for higher accretion rates (tends to a minimum opening angle for cases of very high accretion rates).

Numerical results show that the funnels are insensitive to black hole mass. In this paper, we take $M_\bullet = 10^7 M_\odot$ for most of our calculations.

2.2.2. Anisotropic Radiation Field

Canonical spectra of slim accretion disks have been calculated by Szuszkiewicz et al. (1996), Wang et al. (1999), Mineshige et al. (2000), and Watarai et al. (2005), among others. Previous models approximate the slim disk as parallel layers, and neither the influence of the disk geometry on the emergent spectra nor the ionizing spectra received by the BLR clouds has been investigated. The BLR clouds cannot be regarded as

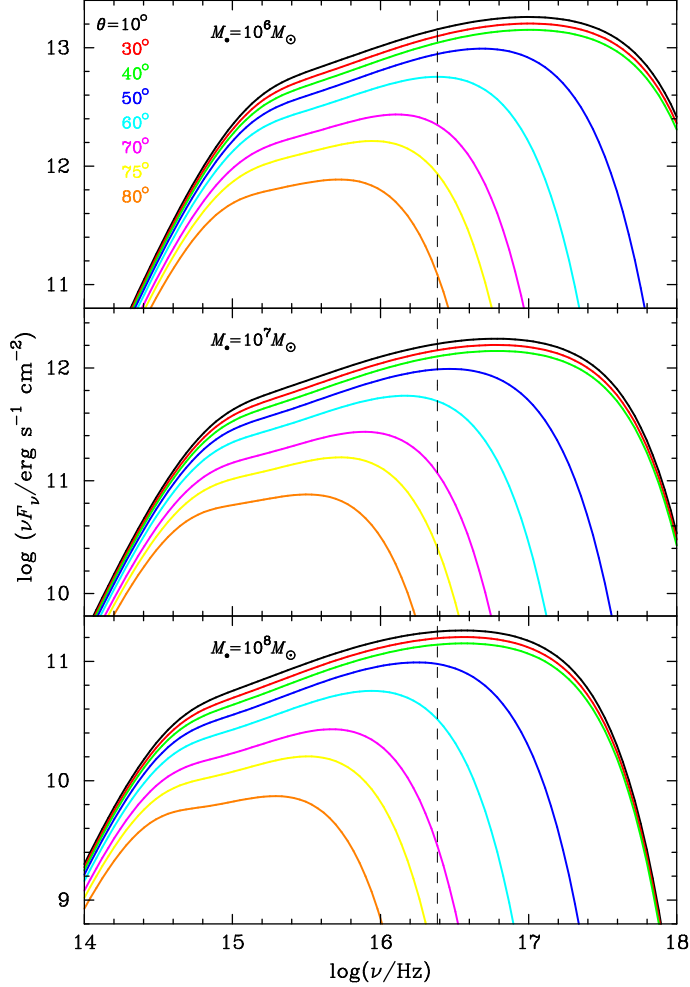


FIG. 4.— Spectral energy distributions of slim disks received by BLR clouds at different angles illustrate the anisotropy of the radiation field from slim disks. Colored lines correspond to the values of parameters labeled with the same color. The orientation angle θ of one cloud in the BLR is defined by $\tan \theta = r_0/z_0$ with respect to the Z-axis. The received SED strongly depends on θ . We assume $\dot{M} = 500$, and the distances of the clouds are assumed to be $r_0 = 10^4 r_g$. There is a clear break frequency in the SED due to photon trapping; it depends on the black hole mass and viewing angle. An observer at high inclinations only receives emission from the parts of the disk without photon trapping, so that the break disappears gradually. The dashed line is 0.1 keV, above which the SED mainly drives H β emission.

a receiver at infinity. Figure 3 illustrates the present scheme for calculating the self-shadowing effects on the clouds. We follow the approach used by Pacharintanakul & Katz (1980). Electron scattering has significant effects on the spectra because the Thomson scattering opacity dominates the free-free absorption so that the radiation can be modified as grey blackbody radiation (e.g., Czerny & Elvis 1987). In this paper, we include the effects of electron scattering on the spectra by simplifying it as modified blackbody radiation from the disk surface (e.g., Szuszkiewicz et al. 1996). The intensity of radiation from the disk surface is given by

$$I_\nu = \frac{2B_\nu(T)}{1 + \sqrt{1 + \kappa_{\text{es}}/\kappa_{\text{ff}}(\nu)}}, \quad (12)$$

where $B_\nu(T)$ is the Planck function and the free-free opacity is

$$\kappa_{\text{ff}}(\nu) = 1.5 \times 10^{25} \rho T^{-3.5} x^{-3} (1 - e^{-x}), \quad (13)$$

where $x = h\nu/kT$, h is the Planck constant, k is the Boltzman constant, and the Gaunt factor is taken to be unity. Here, radiation from the surface is isotropic, such that I_ν is independent of angle. The flux received by a cloud at point $P(r_0, \pi/2, z_0)$

in the YOZ plane is given by

$$F_\nu(r_0, z_0) = \int_{\mathcal{S}_0} I_\nu(r, \phi, z) (\vec{n} \cdot \vec{n}_1) (\vec{n}_1 \cdot \vec{n}_0) \frac{d\mathcal{S}}{d_0^2}, \quad (14)$$

where d_0 is the distance of the cloud to the center, \vec{n}_0 is the direction of the line-of-sight of the cloud in the BLR, \vec{n} is the outward normal to the surface area element $d\mathcal{S} = r(1 + H_r^2)^{1/2} dr d\phi$, \mathcal{S}_0 is the area unobscured by the disk itself, and \vec{n}_1 is the normal vector from any point $P(r, \phi, z)$ of the disk surface. Appendix gives details. It should be noted here that d_0 is not much larger than the disk size, and the shape of the disk is important to calculate the ionizing flux of the BLR clouds.

Figure 4 shows SEDs received by clouds in the BLR with different orientation to the disk. Clouds with $R_0 = 10^4 r_g$ for different viewing angles $\theta = \tan^{-1}(r_0/z_0)$ are considered for slim disks with $\dot{M} = 500$ and $M_\bullet = 10^6, 10^7$, and $10^8 M_\odot$. It clearly shows the anisotropy of the radiation field. Two effects are seen: (1) The flux received by the clouds dramatically decreases with orientation angle by a factor of 30 for $\theta = 10^\circ$ to 80° , which is much steeper than $\cos \theta$; (2) the SEDs are

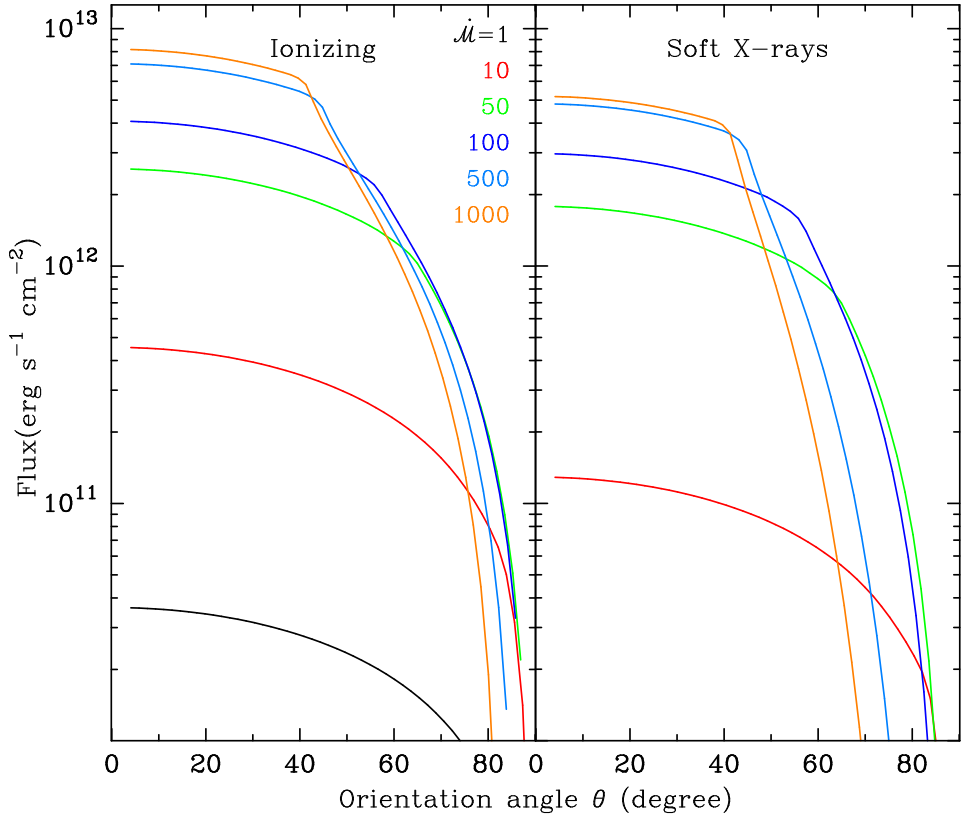


FIG. 5.— The (left) ionizing (photons with energy ≥ 13.6 eV) flux and (right) soft X-ray flux of a slim disk as viewed by BLR clouds at different angles. We find that the flux decreases sharply beyond the half opening angle of the disk funnel. The anisotropy of emissions received by the clouds depends on the orientation angle and accretion rate of the slim disk. Comparing the two panels, we find that soft X-rays are more anisotropic than ionizing (UV + soft X-ray) photons.

significantly softened by self-shadowing at lower latitudes, resulting in the lack of photoionizing photons for emission lines. As a consequence, the clouds are exposed to SEDs and luminosities different from the observer. These two effects may introduce scatter to the $\tau_{\text{BLR}} - L$ relation and may allow an opportunity to relax the energy budget in the BLR. Self-shadowing effects are very crucial for the manner in which BLR clouds respond to the varying continuum.

The theoretical SEDs of slim disks in the optical to UV regime show a characteristic form $F_\nu \propto \nu^{\alpha_\nu}$, with $\alpha_\nu \approx -1$ within the photon trapping radius, spanning a frequency range that depends on accretion rate. Beyond the photon trapping radius, the disk emission approximately follows the standard $\alpha_\nu = +1/3$ shape of an SS disk. The transition frequency between these two regimes (from $\alpha_\nu = +1/3$ to -1) depends on M_\bullet , \dot{M} , and even BH spin. Neither of these naive expectations compares favorably with observations, although the mismatch for SS disks is a well-known problem (e.g., Koratkar & Blaes 1999). Studies of the composite optical-UV SEDs of quasars and AGNs typically find $\alpha_\nu \approx -0.3$ to -0.6 for $\lambda > 1200$ Å, steepening to $\alpha_\nu = -1.4$ to -2 for $\lambda < 1000$ Å (e.g., Zheng et al. 1997; Telfer et al. 2002). The average FUV-EUV slope of the 22 sources recently analyzed by Shull et al. (2012) is $\langle \alpha_\nu \rangle = -0.96 \pm 0.41$, with considerable variation from object to object. This observed slope superficially resembles the characteristically flat spectrum of a slim disk, but we caution against overinterpretation. More sophisticated calculations are needed to produce robust SED predictions for slim disks. Moreover, we do not have complete

information on the Eddington ratios of the objects in Shull et al.’s sample. We emphasize, however, that none of the conclusion of this study depends on knowledge of the detailed SED of a slim disk. Instead, we simply utilize the fact that, due to self-shadowing and the resulting anisotropy, the overall SED exhibits a strong angular dependence, as illustrated in Fig 4.

The ionizing flux for hydrogen atoms is usually defined by $F_{\text{ion}} = \int_{13.6\text{eV}}^{\infty} F_\nu d\nu$. Since H β emissions are mainly driven by soft X-rays (e.g., Kwan & Krolik 1979), we also define $F_{\text{SX}} = \int_{0.1\text{keV}}^{\infty} F_\nu d\nu$. Figure 5 shows the dependence of F_{ion} and F_{SX} on self-shadowing effects. Models are calculated for slim disks with different accretion rates \dot{M} . We find that SS disks have much weaker anisotropy of their radiation fields, which can be roughly approximated by $\cos\theta$, and hence self-shadowing effects can be neglected. Moreover, the ionizing photons tend to saturated with increasing \dot{M} and have strong anisotropy when $\theta \gtrsim \Theta_{\text{fun}}$, which leads to anisotropic illumination of the BLR. Lastly, the anisotropy within the funnels of the slim disk varies with $\cos\theta$, as is the case in thin disks. This can be understood by the fact that the projected area of the funnels is viewed by a factor $\cos\theta$.

For slim disks, the strong anisotropy of the radiation field divides the BLR into two regions marked as Regions I and II in Figure 3. Region I is unshadowed and Region II is shadowed. For slim disks with $\dot{M} = 500$, the ionizing flux ratio $F_i/F_{\text{II}} \sim 5 - 14$ for $\theta = 10^\circ - 40^\circ$ and $\theta = 60^\circ - 70^\circ$. Obviously, this ratio depends on \dot{M} because the self-shadowed re-

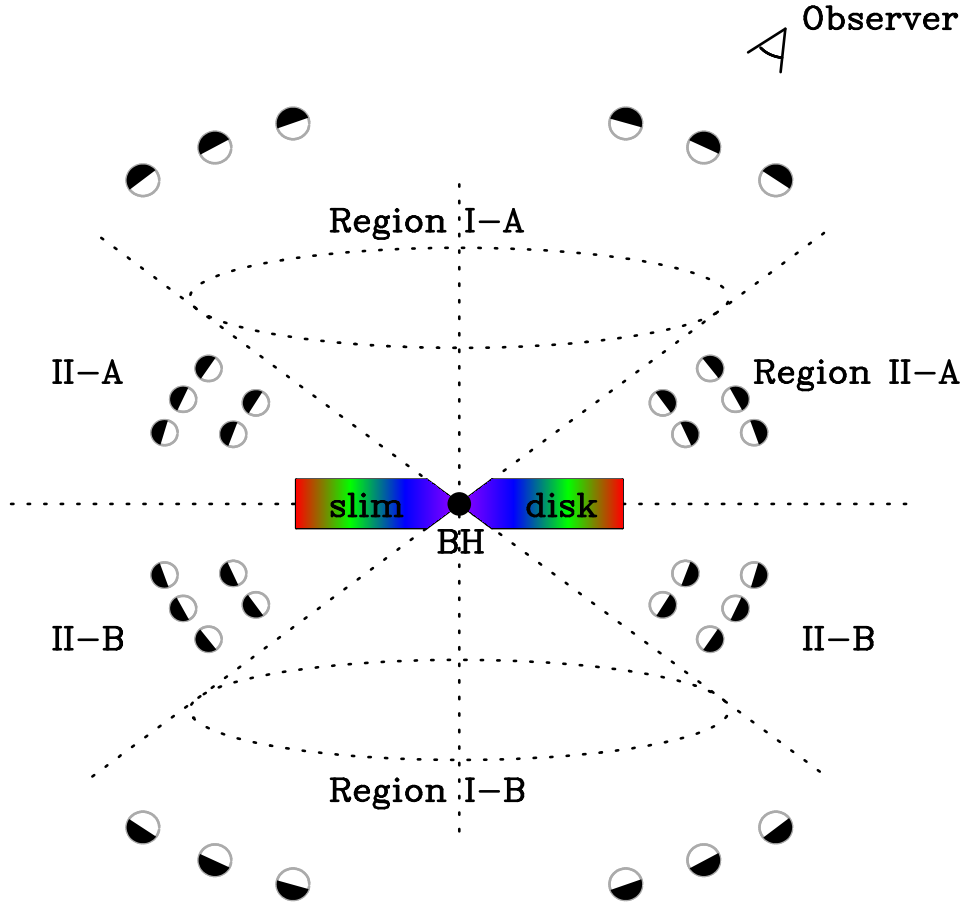


FIG. 6.— A cartoon of the BLR illuminated by a slim disk. Regions I and II are divided by the funnel of the disk. The clouds emit H β photons anisotropically. The inward-facing part of the cloud (white) is ionized, whereas the outward-facing part of the cloud (black) is not ionized. H β photons are only emitted from the inward face. Given the anisotropy of H β emission, we divide the BLR into Regions I-A and I-B and Regions II-A and II-B. The observed H β fluxes in these regions have different contributions in response to the varying continuum. Clouds in the BLR are presumed to be distributed homogeneously around the accretion disk, but the clouds plotted here are only those emitting H β .

gions rely on the funnel opening angle determined by \mathcal{M} . The strong self-shadowing effects on the illumination of the BLR govern diverse observed appearance of the BLR, in particular the H β reverberation with varying continuum.

In this section, we show that the BLR is divided into two regions (I and II) in light of the radiation anisotropy of slim disks. We will show that the clouds in the two regions reverberate differently in response to a varying continuum. We stress the natural appearance of two distinct regions due to the anisotropic radiation from slim disks. In this work, we neglect the reflection of the photons in the funnel of the slim disk. This additional source of heating for the funnel could increase the funnel effects in slim disks. We also do not consider general relativistic effects in the disk structure or photon propagation. All these effects will enhance the self-shadowing effects. The present results should be conservative considerations.

3. OBSERVATIONAL CONSEQUENCES

One of the main goals of the present paper is to show the effects of the anisotropic disk radiation on the BLR in systems with high accretion rates. It is beyond the scope of the present paper to systematically build up a complete model of the BLR; however, we will outline the major consequences of the anisotropic illumination produced by slim disks. Our present discussion has the greatest bearing on NLS1s.

In order to investigate the observational consequences on

the BLR, we have to reasonably postulate some basic physical properties and spatial distribution of the clouds. We assume that a large number of clouds occupy the entire space surrounding the accretion disk. Considering the anisotropic illumination of the clouds, their spatial distribution falls into two regions. The physical properties of the clouds are based on the calculations of Ferland et al. (2009). For clouds with large column density, we simplify the cloud's emission into two parts: (1) the front surface facing the ionizing source and (2) the back facing away from the ionizing source. The former is called inward emission, and the latter is referred to as outward emission. The ratio of inward to outward emission depends on the column density of the clouds.

The photoionization calculations of Ferland et al. (2009) show that, for a typical column density of $N_{\text{H}} \gtrsim 10^{22} \text{ cm}^{-2}$, the outward component of the line intensity is characterized by $I(\text{Fe II})/I(\text{H}\beta)_{\text{tot}} \sim 10$ and $I(\text{H}\beta)_{\text{out}}/I(\text{H}\beta)_{\text{tot}} \sim 0.1$, where $I(\text{H}\beta)_{\text{tot}}$ is the sum of the inward and outward emission. This indicates that optical Fe II emission is isotropic whereas H β emission is anisotropic (Ferland et al. 2009). It is reasonable to assume that the clouds in AGNs with high accretion rates may have large N_{H} . Otherwise, the clouds will be blown away by the super-Eddington luminosity. Additionally, the reverberation response of H β to the varying continuum indicates that the BLR clouds are not fully ionized. We assume

that clouds with large column density ($> 10^{22} \text{ cm}^{-2}$) in Regions I and II emit $\text{H}\beta$ anisotropically but that Fe II is emitted isotropically. However, but we bear in mind that the column density of the clouds is highly uncertain; we will briefly discuss the effects on low- N_{H} clouds.

3.1. Two Dynamical Regions of the BLR

If the BLR has a constant product $n_e U$, we naively expect the size of the BLR to scale with the ionizing luminosity as $R_{\text{BLR}} \propto L_{\text{ion}}^{1/2}$, where L_{ion} is the ionizing luminosity. This size scaling agrees surprisingly well with the reverberation mapping data for $\text{H}\beta$ (Kaspi et al. 2000; Bentz et al. 2013). This luminosity-size relation can be used to constrain the two regions of the BLR affected by the anisotropic illumination (see Figure 3). Considering the high anisotropy of the radiation from slim disks, the size scales of the two BLR regions are related through

$$\frac{R_{\text{BLR,I}}}{R_{\text{BLR,II}}} = \left(\frac{L_{\text{ion,I}}}{L_{\text{ion,II}}} \right)^{1/2} = \left(\frac{F_{\text{ion,I}}}{F_{\text{ion,II}}} \right)^{1/2}, \quad (15)$$

where $F_{\text{ion,I}}$ and $F_{\text{ion,II}}$ are the fluxes⁵ at the typical opening angles at radius $r_0 = 10^4 r_g$. As shown in Figure 3, we have the ratio of $R_{\text{BLR,I}}/R_{\text{BLR,II}} = (2.0, 2.5, 3.5, 4.6)$ for $\dot{M} = (50, 100, 500, 1000)$ and $(\theta_{\text{I}}, \theta_{\text{II}}) = (20^\circ, 70^\circ)$, where $\theta_{\text{I,II}}$ are the orientation angles in Regions I and II. From these calculations, we approximate

$$\frac{R_{\text{BLR,I}}}{R_{\text{BLR,II}}} \approx 2.0 \dot{M}_{50}^{0.3}, \quad (16)$$

where $\dot{M}_{50} = \dot{M}/50$. We point out that the size of the BLR (R_{BLR}) used here is the ionization front of the BLR. In the presence of self-shadowing effects, the ionization front shrinks rather than changes the spatial distributions of clouds. Figure 6 gives a cartoon of the two-region BLR, showing how the $\text{H}\beta$ -emitting clouds in the two regions are located at different distances from the center.

Since the clouds in Regions I and II have different distances from the center, the velocity widths of $\text{H}\beta$ from the two regions should also be different. For lines broadened by the black hole potential, we have

$$\frac{V_{\text{H}\beta,\text{I}}}{V_{\text{H}\beta,\text{II}}} = \left(\frac{R_{\text{BLR,I}}}{R_{\text{BLR,II}}} \right)^{-1/2} \approx 0.7 \dot{M}_{50}^{-0.15}, \quad (17)$$

where V is the full width half-maximum of the $\text{H}\beta$ profile. The clouds in the two regions have different kinematics, such that $V_{\text{H}\beta,\text{I}} < V_{\text{H}\beta,\text{II}}$. This implies that the observed $\text{H}\beta$ emission is composed of two independent components: a very broad component (VBC) with $V_{\text{H}\beta,\text{II}}$ and an intermediate-breadth component (IBC) with $V_{\text{H}\beta,\text{I}}$. The VBC and IBC are dynamically independent. The strong anisotropic radiation indicates that the ratio of the two region sizes, and hence also the ratio of their respective velocity widths, depends on accretion rate.

As illustrated in Figure 6, Regions I and II have altogether four subsections (see the figure caption for a detailed explanation). The separation between Regions II-A and II-B are

⁵ Soft X-rays are the main driver for $\text{H}\beta$ emission, as pointed out by the referee. In the subsequent discussion, F_{ion} represents F_{SX} for $\text{H}\beta$ emission; however, we retain F_{ion} as a general symbol.

caused by the complete shadowing of the slim disk. The total $\text{H}\beta$ emission comes from the four subsections, depending on the observer's orientation with respect to the funnel. We stress that all four subsections contribute to the BLR emission. Real BLRs may be more complicated than the schematic envisioned here, but the main features and consequences of anisotropic illumination of the BLR should be robust.

As $\text{H}\beta$ arises from photoionized clouds, its flux can be written as $F_{\text{H}\beta} = C \eta_{\text{H}\beta} F_{\text{ion}}$, where C is the covering factor of the BLR and $\eta_{\text{H}\beta}$ is the efficiency for reprocessing ionizing photons into $\text{H}\beta$. For simplicity, we assume that the radiation efficiency $\eta_{\text{H}\beta}$ is the same for all clouds. The total observed flux from the four regions is given by

$$F_{\text{H}\beta}^{\text{tot}} = (\xi_{\text{IA}} + \xi_{\text{IB}}) C_{\text{I}} \eta_{\text{H}\beta} F_{\text{ion,I}} + (\xi_{\text{IIA}} + \xi_{\text{IIB}}) C_{\text{II}} \eta_{\text{H}\beta} F_{\text{ion,II}}, \quad (18)$$

where ξ is the anisotropic factor for $\text{H}\beta$ emission, and its subscript refers to the corresponding subsection. These factors depend on the orientation of the observer as well as on the column density of the clouds. For a pole-on observer, we have the characteristic values $\xi_{\text{IA}} = 0$, $\xi_{\text{IB}} = 1$, and $\xi_{\text{IIA}} = \xi_{\text{IIB}} = 1/2$.

If the clouds are distributed homogeneously around the central ionizing source, the covering factor $C_{\text{I}} \propto \Delta\Omega = 2\pi(1 - \cos\Theta_{\text{fun}})$ and $C_{\text{II}} \propto 2\pi\cos\Theta_{\text{fun}}$, where $\Delta\Omega$ is the solid angle subtended by the funnel. The flux ratio of VBC and IBC for $\text{H}\beta$ depends on the covering factors, such that

$$\frac{F_{\text{H}\beta,\text{I}}}{F_{\text{H}\beta,\text{II}}} = \frac{(\xi_{\text{IA}} + \xi_{\text{IB}}) C_{\text{I}} F_{\text{ion,I}}}{(\xi_{\text{IIA}} + \xi_{\text{IIB}}) C_{\text{II}} F_{\text{ion,II}}} = 3.6 \frac{(\xi_{\text{IA}} + \xi_{\text{IB}})(1 - \cos\Theta_{\text{fun}})}{(\xi_{\text{IIA}} + \xi_{\text{IIB}}) \cos\Theta_{\text{fun}}} \dot{M}_{50}^{0.6} \quad (19)$$

for $(\theta_{\text{I}}, \theta_{\text{II}}) = (20^\circ, 70^\circ)$. For pole-on observers, we have $F_{\text{H}\beta,\text{I}}/F_{\text{H}\beta,\text{II}} \approx (\cos^{-1}\Theta_{\text{fun}} - 1) \dot{M}_{50}^{0.6} \approx 0.4 \dot{M}_{50}^{0.6}$, which is a function of \dot{M} . Future tests can be done by evaluating these potential empirical correlations.

For AGNs in the SS regime, self-shadowing is very weak so that the boundary between Regions I and II disappears. Apart from the factor $\cos\theta(1 + 2\cos\theta)$, the effects of anisotropic radiation can be neglected. All the properties discussed in this paper reduce to those of normal (sub-Eddington) AGNs. The two components of the BLR (VBC and IBC) merge together into an approximately single Gaussian profile, consistent with observations of most quasars and Seyfert 1 galaxies.

Note that the condition of constant $n_e U$ in the BLR may not be a unique explanation for the $R_{\text{BLR}} - L$ relation. In the locally optimally emitting cloud model of Baldwin et al. (1995), the ionization parameter as well as the BLR density have a large range of values. An alternative view is that the $R_{\text{BLR}} - L$ relation may result from the effects of dust sublimation in the BLR (Laor & Draine 1993; Netzer & Laor 1993). It is not the goal for the present paper to enter into this debate. We simply employ the $R_{\text{BLR}} - L$ relation to discuss the ionization front of the BLR and how it is anisotropically illuminated by a slim disk. Our results do not depend on the physical interpretation of the $R_{\text{BLR}} - L$ relation.

3.2. $\text{H}\beta$ Reverberation

Obviously, the manner in which $\text{H}\beta$ responds to the varying continuum depends on the properties of the clouds in the four subregions. The actual observed reverberation is an averaged response by the spatial distribution of clouds (or averaged emissivity of the spatial distribution of clouds). We discuss here the characteristic time lags of the BLR. Decomposing the VBC and IBC of $\text{H}\beta$, we find that the two components should have different lags. Consider that the $\text{H}\beta$ emission

from clouds in Region I-A is invisible while that from Region I-B is visible and reverberates with the varying continuum. Reverberation of $H\beta$ has a lag of $R_{\text{BLR},\text{I}}(1+\cos\langle\Theta_{\text{I}}\rangle)/c$ with the continuum, where $\langle\Theta_{\text{I}}\rangle$ is the mean orientation angle of clouds in Region I. Following Kaspi et al. (2000), we assume $\tau_0 = R_{\text{BLR},\text{I}}/c$, and, hence, for a pole-on observer,

$$\tau_{H\beta,\text{I}} = (1+\cos\langle\Theta_{\text{I}}\rangle)\tau_0 \approx 2\tau_0, \quad (20)$$

which, for small $\langle\Theta_{\text{I}}\rangle$, is significantly longer than τ_0 . This longer lag is caused jointly by the anisotropic emission of $H\beta$ and the funnel effect. This is very significant for observational tests.

Clouds in Region II are located at low altitudes. Although $H\beta$ emission is anisotropic, the inward emission of $H\beta$ from most clouds will be visible. The time lag of $H\beta$ from Region II-B can be approximated by $R_{\text{BLR},\text{II}}(1+\cos\langle\Theta_{\text{II}}\rangle)/c$, where $\langle\Theta_{\text{II}}\rangle$ is the average orientation angle of clouds in Region II. Clouds in Region II-A are visible. The $H\beta$ lags from Region II-A cannot be longer than $R_{\text{BLR},\text{II}}(1-\cos\langle\Theta_{\text{II}}\rangle)/c$, while the clouds in Region II-B cannot be shorter than $R_{\text{BLR},\text{II}}(1+\cos\langle\Theta_{\text{II}}\rangle)/c$. This indicates that the VBC has two lags in response to continuum variability, implying that the cross correlation function of the VBC should have two peaks. The ratio of the two peaks measured by a pole-on observer is given by

$$\frac{\tau_{H\beta,\text{IIA}}}{\tau_{H\beta,\text{IIB}}} = \frac{1+\cos\langle\Theta_{\text{II}}\rangle}{1-\cos\langle\Theta_{\text{II}}\rangle}, \quad (21)$$

in which $\langle\Theta_{\text{II}}\rangle$ is a function of \dot{M} . For the extreme case in which $\langle\Theta_{\text{II}}\rangle \approx 3\pi/8$ (i.e., the average angle between $\pi/4$ and $\pi/2$), we have $\tau_{H\beta,\text{IIA}}/\tau_{H\beta,\text{IIB}} \approx 2.2$. This results purely from the effects of the anisotropic illumination of slim disks. When the illumination is homogeneous, the two peaks will merge. Considering the symmetric distribution of clouds in Regions II-A and II-B, the ratio is independent of the covering factor of the regions and is only sensitive to the orientation angles of Region II. This sensitivity provides an opportunity to observationally measure the orientation angle. This suggested effect is based on the fact that clouds in Region II have a large column density to reverberate with the varying continuum.

Comparing the time lags between Regions I and II, we have the following ratios:

$$\frac{\tau_{H\beta,\text{I}}}{\tau_{H\beta,\text{II}}} = \begin{cases} \frac{1+\cos\langle\Theta_{\text{I}}\rangle}{1+\cos\langle\Theta_{\text{II}}\rangle} \left(\frac{R_{\text{BLR},\text{I}}}{R_{\text{BLR},\text{II}}} \right) \approx 3\dot{M}_{50}^{0.3}, \\ \frac{1+\cos\langle\Theta_{\text{I}}\rangle}{1-\cos\langle\Theta_{\text{II}}\rangle} \left(\frac{R_{\text{BLR},\text{I}}}{R_{\text{BLR},\text{II}}} \right) \approx 6\dot{M}_{50}^{0.3}, \end{cases} \quad (22)$$

for $\langle\Theta_{\text{I}}\rangle = 20^\circ$ and $\langle\Theta_{\text{II}}\rangle = 70^\circ$. Equation (22) includes two kinds of reverberations described by Equation (20) and (21). It is very important that the ratios depend on the dimensionless accretion rate \dot{M} . We note that the radiated luminosity tends to be saturated for SEAMBHs, and the SEDs will be insensitive to \dot{M} . This makes it very difficult to constrain the true value of \dot{M} . Fortunately, the ratio of fluxes and time lags of $H\beta$ emission are mildly sensitive to \dot{M} , and so we may be able to constrain \dot{M} from monitoring the two components of $H\beta$ emission. Equation (22) provides a useful way to estimate \dot{M} , through the numerical approximation

$$\ln \dot{M}_{50} = 3 \ln(\tau_{H\beta,\text{I}}/\tau_{H\beta,\text{II}}) - 4.6. \quad (23)$$

The above discussion assumes that the ionized clouds in Region I emit anisotropically, which may or may not strictly hold in all cases. Nevertheless, we expect that on average the clouds in Region I will have longer lags than those in Region II. We further assumed that the clouds in Region II are not fully ionized. If the ionization parameter in Region II is much higher than that in Region I, $H\beta$ from Region II may not reverberate. In such a case, while both VBC and IBC are present in the composite line profile, only the IBC will respond to variations in the ionizing continuum.

3.3. The $\tau_{\text{BLR}} - L$ Relation

The $R_{\text{BLR}} - L$ relation (Kaspi et al. 2000; Bentz et al. 2013) is roughly consistent with the BLR having a constant $n_e U$. The observed tightness of the relation, strongly suggests that the ionizing continuum received by the BLR clouds is the same as that seen by the observer. Indeed, most of the ~ 50 reverberation-mapped AGNs are sub-Eddington systems, whose SS disk is not expected to produce strong anisotropic emission. Super-Eddington AGNs, however, being strongly affected by the self-shadowing effects discussed in this work, produce broad-line emission from two distinctive regions, each with a different lag. The observed lag is the sum of the lags from Regions I and II.

If the $H\beta$ emission is not decomposed into the VBC and IBC, the lag of the total $H\beta$ flux $F_{H\beta}^{\text{tot}}$ can be determined by the cross correlation function,

$$\begin{aligned} \text{CCF} &= F_{H\beta}^{\text{tot}} \otimes F_{\text{ion},\text{I}} \\ &\propto (\xi_{\text{IA}} + \xi_{\text{IB}}) C_{\text{I}} f_1(t, \tau_{\text{I}}) + (\xi_{\text{IIA}} + \xi_{\text{IIB}}) C_{\text{II}} q f_2(t, \tau_{\text{II}}), \end{aligned} \quad (24)$$

where $q = F_{\text{ion},\text{I}}/F_{\text{ion},\text{II}}$ is the ratio of fluxes in the two regions, $F_{H\beta,\text{I}}(t) = C_{\text{I}} \eta_{H\beta} F_{\text{ion},\text{I}}(t - \tau_{\text{I}})$, $F_{H\beta,\text{II}}(t) = C_{\text{II}} q \eta_{H\beta} F_{\text{ion},\text{II}}(t - \tau_{\text{II}})$, $f_1(t, \tau_{\text{I}}) = F_{\text{ion},\text{I}} \otimes F_{\text{ion},\text{I}}(t - \tau_{\text{I}})$ and $f_2(t, \tau_{\text{II}}) = F_{\text{ion},\text{II}} \otimes F_{\text{ion},\text{II}}(t - \tau_{\text{II}})$ are the autocorrelation functions with peaks at τ_{I} and τ_{II} , which are the lags of the two components. Here we note that the observed continuum only comes from Region I for observers with small θ . The observed lag is the averaged values of τ_{I} and τ_{II} , which are governed by the covering factors of Regions I and II and the anisotropy (ξ) of $H\beta$ emission from the BLR clouds. Since the covering factors are related to the fluxes of the two components and \dot{M} (see eq. 8), for extremely high accretion rates C_{II} may dominate C_{I} , in which case τ_{II} can be significantly shorter than the lag predicted from the $\tau_{\text{BLR}} - L$ relation. Therefore, we predict that super-Eddington sources should significantly deviate from the normal $\tau_{\text{BLR}} - L$ relation.

The ratios of fluxes and lags of the two components depend on the funnel opening angle and accretion rate. Future reverberation mapping observations can be analyzed in detail to constrain the funnel opening angle and accretion rate. This can be achieved in practice for actual reverberation mapping data. Note that the timescale of Keplerian rotation is given by $t_{\text{Kep}} \approx 10 m_7 r_4^{3/2}$ yr, where $r_4 = r/10^4 r_{\text{g}}$. This timescale is much longer than typical monitoring periods (about 6 months), and thus the individual regions should retain stable emission profiles during the course of an observational campaign.

Current models do not provide strong constraints on the BLR covering factor. The relationship between the SED of an AGN and the properties of the BLR clouds has been discussed by Fabian et al. (1986) and Bechtold et al. (1987) in the context of the two-phase model of quasar emission-line

regions (Krolik et al. 1981). The preliminary discussion on anisotropic effects by Bechtold et al. (1987), interestingly, is based on the NLS1 PG 1211+143. Goad & Wanders (1996) investigate some effects of anisotropic illuminations on the BLR clouds. It has been observationally well established that accretion disks with higher accretion rates have fainter hard X-rays than ones with lower rates because of Comptonization of the hot corona by efficient cooling (e.g., Wang et al. 2004; Kelly et al. 2008; Cao 2009; Uzdensky 2013; see also Czerny et al. 2003; Proga 2005). This property holds in AGNs and quasars, from low to high redshifts (e.g., Shemmer et al. 2008; Brightman et al. 2013; Fanali et al. 2013). In such a case when the ionizing spectrum is very soft, the lower Compton temperature and enhanced cooling may actually inhibit the existence/formation of clouds within the funnel (Krolik et al. 1981). The covering factor (C_i and C_{ii}) and its variation with angle from the disk axis should be obtained self-consistently from models that employ the SEDs of slim disks.

3.4. Reverberation of Fe II Emission

AGNs with high accretion rates are known to have strong iron (Fe II) lines in the optical and UV bands (e.g., Boroson 2002). A systematic study of Sloan Digital Survey (SDSS) quasars shows that Fe II emission has FWHM and velocity offsets similar to the intermediate-width component of H β (Hu et al. 2008a,b, 2012). This velocity offset anti-correlates with the Eddington ratio, so that it vanishes for most NLS1s. Generally, however, it has been difficult to detect variability in Fe II emission in AGNs. Barth et al. (2013) recently reported Fe II variability and a successful determination of its time lag in two AGNs; the Fe II lag is longer than that of H β by a factor of ~ 2 . With the goal of studying the properties of SEAMBHs, Du et al. (2014) and Wang et al. (2014) have been carrying out a large campaign to monitor AGNs and quasars with high accretion rates. Detailed analysis of Fe II will be carried out in a separate paper (C. Hu et al. 2014, in preparation), but here we note that the longer lags expected for Fe II are generally consistent with the predictions of our simple model. For clouds with large N_H , Fe II $\lambda 4558$ Å emission is isotropic and the observed Fe II strength increases with \dot{M} (see Figure 3 in Ferland et al. 2009). However, the UV complex Fe II $\lambda 2445$ Å emits predominantly inward due to its large optical depth. We expect Fe II $\lambda 2445$ Å to reverberate with a longer lag than Fe II $\lambda 4558$ Å. This may explain why Fe II $\lambda 4558$ Å is strong whereas Fe II $\lambda 2445$ Å is expected to reverberate later than Fe II $\lambda 4558$ Å with the continuum. The different behavior of Fe II in the optical and UV bands can be tested observationally using simultaneous observations.

As we argued in the last paragraph of §3.1, it is possible that Region II has high U . A high U in Region II suppresses Fe II emission relative to Region I. This prediction of our model indicates that Fe II variations follow the IBC and reverberate with the varying continuum. To date, only two AGNs have been successfully monitored for Fe II variations (Barth et al. 2013), and neither is powered by a slim disk. A key test of our present model is to monitor the Fe II variations and check if they follow the varying continuum.

3.5. BLR and Outflows

The scaled distances of the BLR ionization fronts are based on the paradigm of a constant product $n_e U$. However, this has

additional effects on the clouds⁶. The self-shadowing effects may lower the gas pressure of the surrounding medium of the clouds in the shadowed regions so that the internal pressure causes the clouds to expand from r_{cl}^0 to r_{cl} . For mass conservation to hold, the column density of clouds in the shadowed regions changes as $N_H = N_H^0 (r_{cl}^0 / r_{cl})^2$, where N_H^0 is the column density of the unshadowed regions. The column density of the clouds in Region II is lower than that in Region I so that the clouds in Region II may transition from $\tau \gg 1$ to $\tau \sim 1$; this speculation needs to be verified with future detailed calculations. The case of $\tau \gg 1$ clouds in Region II has been discussed in previous sections. What about the potential situation of $\tau \lesssim 1$ clouds? Each cloud may be mostly ionized, and the H β flux depends on the reprocessing efficiency of the clouds. More interesting, clouds in Region II may undergo acceleration driven by line radiation pressure with a large force multiplier to produce outflows from this region. Observationally, the VBC is expected to show blueshifts and reverberate little, if at all, with the continuum.

If clouds are blown away in Region II, how are they replenished? According to numerical simulations, slim accretion disks develop strong outflows (Ohsuga et al. 2005; McKinney et al. 2014; Sadowski et al. 2014), which may be the very source of clouds for the BLR (Murray & Chiang 1997; Kashi et al. 2013). This physical picture in principle can be tested directly through velocity-resolved (two-dimensional) reverberation mapping, which can help to diagnose the dynamics of the BLR (Denney et al. 2009, 2010; Grier et al. 2013). However, as we argue below, velocity-resolved reverberation mapping technique is still limited because it is not able to uniquely map the velocity field in space. For AGNs with extremely high accretion rates, fortunately, self-shadowing effects provide an opportunity to probe the connection between outflows and the BLR through the different reverberation properties of clouds in Regions I and II, which can be decomposed as separate components of the H β line.

In principle, we can estimate the outflow rates from the disk surface if we can detect shifts (V_{out}) of the VBC (Region II) from reverberation mapping observations. The radius of the outflow can be estimated by the size of the VBC region, $R_{BLR,II}$, and hence the mass outflow rate

$$\dot{M}_{out} = 2\pi R_{BLR,II}^2 V_{out} C_{ii} \rho_c, \quad (25)$$

where ρ_c is the mass density of the emitting clouds. In principle, C_{ii} can be determined from the equivalent width of the VBC, and ρ_c can be estimated from photoionization calculations. If the outflow is composed of discrete clouds, $C_{ii} \rho_c$ is the average density of the outflow. Previous attempts to obtain mass outflow rates in AGNs, for example from UV absorbers (e.g., Arav et al. 2013), have been frustrated mainly by the lack of reliable distance estimates. The method proposed here solves this problem because R_{VBC} can be determined accurately by reverberation mapping. Comparing \dot{M}_{out} with \dot{M}_\bullet , we can set rigorous constraints on the theoretical model of slim disks from observations.

We bear in mind that clouds in Region I may be fully ionized and have no reverberation with the varying continuum.

⁶ The existence of clouds in the two-phase BLR model (Krolik et al. 1981) is often questioned because of the expected short lifetimes of the clouds due to dynamical friction in the hot medium (Mathews & Ferland 1987). Non-steady models of the BLR avoid this difficulty because the number of clouds is set through the balance between cloud production and cloud destruction in the hot medium (Czerny & Hryniewicz 2011; Wang et al. 2012).

In that case, an outflow would develop within the solid angle of the funnel. Needless to say, improved velocity-resolved reverberation mapping should be applied to test whether the IBC shows any evidence for velocity shifts.

3.6. The Lorentzian Profile of $H\beta$

Apart from the different reverberation response of $H\beta$ from Regions I and II expected in the time domain, the single-epoch spectra of AGNs powered by slim disks may exhibit kinematic signatures that distinguish them from AGNs with lower accretion rates. The $H\beta$ profiles of NLS1s are close to Lorentzian (e.g., Zhou et al. 2006), but the reason for this is insufficiently understood. The Lorentzian profile may depend on the rotation, inflows, outflows, turbulence, and even the orientation of the BLR to the observer (see Kollatschny & Zetl 2011). A Lorentzian profile in principle can be decomposed mathematically into two distinct Gaussian components, which plausibly may be related to the two regions invoked in our scenario. The highly anisotropic illumination of slim disks naturally predicts this type of two-component structure of the BLR. Reverberation mapping provides a promising method to decouple these two components in the time domain.

Velocity-resolved reverberation mapping, which identifies the lags of different parts of the line profile with the varying continuum, has been applied to infer the dynamical structure of the BLR (e.g., Denney et al. 2009, 2010). This idea generally works if the velocity field of the BLR clouds is not degenerate with respect to their spatial distribution. However, the velocity field does not uniquely map to the spatial domain because the observer only views the velocity projected along the line of sight. For example, the core of the $H\beta$ profile may come from different regions of the BLR. This limits the application of velocity-resolved reverberation mapping to reconstruct the BLR, in particular for high-accretion rate AGNs. By contrast, the decomposition of the $H\beta$ emission into two components allows us to get time lags for the two different regions of the BLR. Current Markov Chain Monte Carlo analysis of AGN light curves employed to estimate black hole masses and BLR dynamics assumes that the BLR is homogeneous (Pancoast et al. 2011; Li et al. 2013). Future improvements of this technique should include the inhomogeneous illumination of the BLR.

4. DISCUSSION

4.1. Narrow-line Region

The [O III] $\lambda 5007$ emission line is a prominent feature in the spectra of AGNs and quasars (e.g., Vanden Berk et al. 2001), but it is generally relatively weak in NLS1s (Osterbrock & Pogge 1985; Boller et al. 1996) and especially in systems with high accretion rates (Boroson 2002; Shen & Ho 2014). The inverse correlation between the strength of the narrow lines and Eddington ratio holds not only for [O III] but also for other high-ionization narrow lines (Shen & Ho 2014). The fundamental reason why the amount of narrow-line emission is connected with the accretion rate is still unclear.

Here we suggest that the suppression of high-ionization narrow-line emission with increasing Eddington ratio arises naturally from the strong anisotropy of the ionizing radiation field of slim disks. The deep funnel of the disk confines the ionization cone to illuminate only a portion of the narrow-line region, thus reducing the strength of the narrow lines, especially those of high ionization. This explanation agrees with the interpretation of “Eigenvector 1,” as suggested by Boroson & Green (1992). Usually the ionization cone of [O III]

is thought to be determined by the dusty torus (e.g., Schmitt et al. 2003; Bennert et al. 2006). Here we propose that the collimation begins on much smaller scales, and that it is fundamentally connected with the structure of slim disks. This idea can be tested by measuring the opening angle of ionization cones in AGNs with well-resolved narrow-line regions⁷.

Additionally, the [O III] profile of NLS1s often has blue wings (e.g., Boroson 2005). With Eddington ratios of ~ 2 (equation 2), we would like to point out that slim disks may generate radiation pressure-driven outflows on large scales (e.g., King et al. 2011; Pounds & King 2013). Large-scale outflows driven by slim disks may also explain the correlation between extended radio emission and blue-asymmetric [O III] lines seen in obscured luminous quasars (e.g., Stocke et al. 1992; Zakamska & Greene 2014).

4.2. Weak-line Quasars

Some quasars with nearly featureless spectra have been found in SDSS (e.g., Plotkin et al. 2010); their physical nature is not understood. X-ray observations of radio-quiet weak-line quasars show that they have steeper spectra in the 2-10 keV band and an order of magnitude fainter X-ray emission than normal quasars (Wu et al. 2011, 2012). Empirically it has been established that the steepness of the X-ray slope correlates with Eddington ratio (e.g., Lu & Yu 1999; Wang et al. 2004). This can be understood phenomenologically by appealing to more efficient Compton cooling of the hot corona by seed photons from the cold part of the disk in systems with high accretion rates. This not only steepens the X-ray spectrum but also reduces the output of hard X-rays. Slim disks may naturally suppress thermal instabilities and prevent the formation of a two-phase medium, thus suppressing strong line emission. Furthermore, self-shadowing obscures the X-rays from the hot corona of the disk surface and enhances the suppression of the instabilities. These two factors reduce the strength of the line emission and may explain the appearance of weak-line quasars. As a specific example, the narrow-line quasar PHL 1811, which has X-ray spectral properties very similar to those of NLS1s, has a very soft SED and shows relatively weak emission lines in the optical and UV bands (Leighly et al. 2007). We attribute the weak line emission in PHL 1811 to the self-shadowing effects of its slim disk. Alternatively, Laor & Davis (2011) suggest that the suppressed line emission of weak-line quasars can be explained by the low temperature of the accretion disks around very massive black holes. This hypothesis can be tested with detailed multiwavelength characterization of the SEDs and accurate black hole mass measurements.

4.3. Near-infrared Reverberation with the Varying UV Continuum

The well-known relation between reverberation in the near-infrared (τ_{NIR}) with the varying optical-UV continuum in AGNs (Suganuma et al. 2006) is consistent with the sublimation radius of dust particles evaporated by a central UV source,

$$r_{\text{torus}} = 0.13 L_{44}^{1/2} T_{1800}^{-2.8} \text{ pc}, \quad (26)$$

⁷ Since most Seyfert 1 galaxies are relatively face-on sources, projection effects will be significant. [O III] cones are observed more often in Seyfert 2 galaxies. Only a few of NLS1s (Akn 564, Mrk 493, Mrk 1044, NGC 4051, NGC 5506, NGC 7469, and Mrk 766) have [O III] images (Schmitt et al. 2003; Fischer et al. 2013), so that it is currently difficult to make a statistical test.

where $L_{44} = L_{\text{UV}}/10^{44} \text{ erg s}^{-1}$ is the UV luminosity of the central energy source and $T_{1800} = T/1800 \text{ K}$ is the evaporation temperature of dust particles (Barvainis 1987). This reverberation relation results from the reprocessed emission of the UV radiation from the central disk. It is interesting to note that it also sets up strong constraints on the BLR (Netzer & Laor 1993). However, the self-shadowing effects of slim disks, if the opening angle of the funnel is smaller than the opening angle of the torus, reduces the heating of the inner edge of the torus, leading to a general shrinking of its inner radius. This potential effect has been noted by Kawaguchi (2013) but has yet to be observed. It would be interesting to systematically study the near-infrared reverberation to the optical and UV emission in AGNs with high accretion rates. If the above picture holds, the time lags in the near-infrared will be much shorter than those predicted by the $\tau_{\text{NIR}} - L_{\text{UV}}$ relation of Suganuma et al. (2006).

4.4. Dust-poor or Dust-free Quasars

Hot dust particles are a generic constituent of the dusty torus invoked in AGN unification schemes (Antonucci 1993), and they should emit strong infrared emission (Pier & Krolik 1993). This basic expectation is borne out in many infrared observations of AGNs (e.g., Neugebauer et al. 1987; Haas et al. 2003; Hatziminaoglou et al. 2008). However, there is growing evidence for a minority of quasars that appear to be dust-poor (Hao et al. 2011) or even dust-free (Jiang et al. 2010). Are these systems really deficient in dust?

The self-shadowing effects from slim disks may provide a simple and natural explanation for this class of objects. Again, if the funnel opening angle is smaller than that of the dusty torus, the torus will not be effectively irradiated by the disk. Further, if the torus is supported by the radiation of the accretion disk (Pier & Krolik 1992), it may collapse in the presence of self-shadowing effects from a slim disk, further reducing the ability for the torus to be illuminated by the disk. The torus will thus be infrared-faint and appear to be dust-poor, or even dust-free.

A key observational test of our alternative scenario for the origin of infrared-weak quasars is to quantify the metallicity of the BLR using the UV line diagnostics suggested by Hamann & Ferland (1999). If a quasar is genuinely dust-poor, we expect it also to be metal-poor, to the extent that metal and dust content scale with each other in galaxies (e.g., Draine et al. 2007). In our scenario, infrared-weak quasars

are only apparently dust-poor because the UV photons do not intercept the torus due to the geometric configuration of slim disks. They should, in fact, have normal dust content, and hence normal metal content.

5. CONCLUSIONS

Based on the vertically averaged equations of an accretion flow in the super-Eddington regime, we show that the structure of slim disks contains a sharp inner funnel and a flattened outer region that produces strong self-shadowing and anisotropy of the radiation field. We calculate the SEDs received by clouds located at different orientations in the BLR and show that the anisotropy of the radiation field increases with accretion rate. This allows us to naturally link the structure of the central engine and the BLR in AGNs. We demonstrate that self-shadowing leads to anisotropic illumination of the BLR clouds, which leads to diverse observational properties of broad emission lines such as $\text{H}\beta$ and Fe II . The strong anisotropy of the radiation field naturally divides the BLR into two regions, which have kinematically distinct line widths and temporal response to continuum variations. These predictions can be tested with reverberation mapping of AGNs with high accretion rates (e.g., NLS1s).

We also extensively discuss other observational consequences of the self-shadowing effects of slim disks in AGNs. These include: departures from the relationship between BLR size and luminosity; longer time lags for reverberation of Fe II ; the Lorentzian profile of broad $\text{H}\beta$ in NLS1s; suppression of high-ionization narrow emission lines in systems with high Eddington ratios; origin of weak-line quasars; and reduction of infrared emission from the dusty torus, which can explain apparently dust-poor or dust-free objects.

JMW thanks H. Netzer for useful discussions and suggestions. The authors are grateful to the second referee for his/her helpful reports to improve the paper. The authors are grateful to the members, in particular, C. Hu and Y.-R. Li, of IHEP AGN group for stimulating discussions. J.-Q. Ge is thanked for plotting Figures 3 and 6. This research is supported by the Strategic Priority Research Program – The Emergence of Cosmological Structures of the Chinese Academy of Sciences, Grant No. XDB09000000, by NSFC grants NSFC-11173023, NSFC-11133006, and NSFC-11233003, and by Israel-China ISF-NSFC grant 83/13. LCH receives support from the Kavli Foundation and Peking University.

REFERENCES

Abramowicz, M. A., Czerny, B., Lasota, J.-P., & Szuszkiewicz, E. 1988, *ApJ*, 332, 646

Antonucci, R. R. J. 1993, *ARA&A*, 31, 473

Arav, N., Barlow, T. A., Laor, A., & Blandford, R. D. 1997, *MNRAS*, 288, 1015

Arav, N., Barlow, T. A., Laor, A., Sargent, W. L. W., & Blandford, R. D. 1998, *MNRAS*, 297, 990

Arav, N., Borguet, B., Chamberlain, C., Edmonds, D., & Danforth, C. 2013, *MNRAS*, 436, 3286

Baldwin, J., Ferland G., Korista K., & Verner D. 1995, *ApJ*, 455, L119

Barth, A. J., Pancoast, A., Bennert, V. N., et al. 2013, *ApJ*, 769, 128

Barvainis, R. 1987, *ApJ*, 320, 537

Bechtold, J., Czerny, B., Elvis, M., Fabbiano, G., & Green, R. F. 1987, *ApJ*, 314, 699

Bennert, N., Jungwiert, B., Komossa, S., Haas, M., & Chini, R. 2006, *A&A*, 459, 55

Bentz, M. C., Denney, K. D., Grier, C. J., et al. 2013, *ApJ*, 767, 149

Boller, Th., Brandt, W. N., & Fink, H. 1996, *A&A*, 305, 53

Boroson, T. A. 2002, *ApJ*, 565, 78

Boroson, T. A. 2005, *AJ*, 130, 381

Brightman, M., Silverman, J., Mainieri, V., et al. 2013, *MNRAS*, 433, 248

Cao, X. 2009, *MNRAS*, 394, 207

Chen, L.-H., & Wang, J.-M. 2004, *ApJ*, 614, 101

Czerny, B., & Elvis, M. 1987, *ApJ*, 321, 305

Czerny, B., & Hrynekiewicz, K. 2011, *A&A*, 477, 419

Czerny, B., Niokałuk, M., Różańska, A., et al. 2003, *A&A*, 412, 317

Denney, K. D., Peterson, B. M., Pogge, R. W., et al. 2009, *ApJ*, 704, L80

Denney, K. D., Peterson, B. M., Pogge, R. W., et al. 2010, *ApJ*, 721, 715

Desroches, L.-B., Greene, J. E., & Ho, L. C. 2009, *ApJ*, 698, 1515

Draine, B. T., Dale, D. A., Bendo G., et al. 2007, *ApJ*, 663, 866

Du, P., Hu, C., Lu, K.-X., et al. 2014, *ApJ*, 782, 45

Fabian, A. C., Guibert, P. W., Arnaud, K. A., et al. 1986, *MNRAS*, 218, 457

Fanali, R., Caccianiga, A., Severgnini, P., et al. 2013, *MNRAS*, 433, 648

Ferland, G. J., Hu, C., Wang, J.-M., et al. 2009, *ApJ*, 707, L82

Fischer, T. C., Crenshaw, D. M., Kraemer, S.B., & Schmitt, H. R. 2013, *ApJS*, 209, 1

Frank, J., King, A. R., & Raine, D. J. 2002, *Accretion Power in Astrophysics: Third Edition* (Cambridge: Cambridge Univ. Press)

Goad, M. & Wanders, I. 1996, *ApJ*, 469, 113

Grier, C. J., Peterson, B. M., Horne, K., et al. 2013, *ApJ*, 764, 47

Grupe, D., Komossa, S., Leighly, K. M., & Page, K. L. 2013, *ApJS*, 187, 64

Haas, M., Klaas, U., Müller, S. A. H., et al. 2003, *A&A*, 402, 87

Hamann, F., & Ferland, G. J. 1999, *ARA&A*, 37, 487

Hao, H., Elvis, M., Civano, F., & Lawrence, A. 2011, *ApJ*, 733, 108

Hatziminaoglou, E., Fritz, J., Franceschini, A., et al. 2008, *MNRAS*, 386, 125

Ho, L. C. 2008, *ARA&A*, 46, 475

Hoshi, R. 1977, *Prog. Theor. Phys.*, 58, 1191

Hu, C., Wang, J.-M., Ho, L. C., et al. 2008a, *ApJ*, 683, L115

Hu, C., Wang, J.-M., Ho, L. C., et al. 2008b, *ApJ*, 687, 78

Hu, C., Wang, J.-M., Ho, L. C., et al. 2012, *ApJ*, 760, 126

Jiang, L., Fan, X., Brandt, W. N., et al. 2010, *Nature*, 464, 380

Jiang, Y.-F., Stone, J. & Davis, S. 2014, *ApJ*, arXiv:1410.0768

Jin, C. C., Done, C., Ward, M., Gierliński, M., & Mullaney, J. 2009, *MNRAS*, 398, L16

Kashi, A., Proga, D., Nagamine, K., Greene, J., & Barth, A. J. 2013, *ApJ*, 778, 50

Kaspi, S., Smith, P. S., Netzer, H., et al. 2000, *ApJ*, 533, 631

Kawaguchi, T. 2013, arXiv:1306.0188

Kawaguchi, T., Pierens, A., & Huré, J.-M. 2004, *A&A*, 415, 47

Kelly, B. C., Bechtold, J., Trump, J. R., Vestergaard, M., & Siemiginowska, A. 2008, *ApJS*, 176, 355

King, A. R., Zubovas, K. & Power, C. 2011, *MNRAS*, 415, L6

Kollatschny, W. & Zetral, M. 2009, *Nature*, 470, 366

Koratkar, A. P., & Blaes, O. 1999, *PASP*, 111, 1

Krolik, J. H., McKee, C. F., & Tarter, C. B. 1981, *ApJ*, 249, 422

Kwan, J. & Krolik, J. H. 1979, *ApJ*, 233, L91

Laor, A., & Draine, B. T. 1993, *ApJ*, 402, 441

Laor, A., & Davis, S. 2011, *MNRAS*, 417, 681

Leighly, K. M., Halpern, J. P., Jenkins, E. B., & Casebeer, D. 2007, *ApJS*, 173, 1

Li, G.-X., Yuan, Y.-F. & Cao, X. 2010, *ApJ*, 715, 623

Li, Y.-R., Wang, J.-M., Ho, L. C., Du, P., & Bai, J.-M. 2013, *ApJ*, 779, 110

Lu, Y., & Yu, Q. 1999, *ApJ*, 526, L5

Madau, P. 1988, *ApJ*, 327, 116

Mathews, W., & Ferland, G. J. 1987, *ApJ*, 323, 456

Matsumoto, R., Kato, S., Fukue, J., & Okazaki, A. T. 1984, *PASJ*, 36, 71

McKinney, J. C., Tchekhovskoy, A., Sadowski, A., & Narayan, R. 2014, *MNRAS*, 441, 3177

Mineshige, S., Kawaguchi, T., Takeuchim M., & Hayashida, K. 2000, *PASJ*, 52, 499

Muchotreb, B., & Paczyński, B. 1982, *AcA*, 32, 1

Murray, N., & Chiang, J. 1997, *ApJ*, 474, 91

Netzer, H. 1987, *MNRAS*, 225, 55

Netzer, H. 2013, *Physics of Active Galactic Nuclei* (Cambridge: Cambridge Univ. Press)

Netzer, H., & Laor, A. 1993, *ApJ*, 404, L51

Neugebauer, G., Green, R. F., Matthews, K., et al. 1987, *ApJS*, 63, 615

Ohsuga, K., Mori, M., Nakamoto, T., & Mineshige, S. 2005, *ApJ*, 628, 368

Osterbrock, D. E., & Mathews, W. G. 1986, *ARA&A*, 24, 171

Osterbrock, D. E., & Pogge, R. W. 1985, *ApJ*, 297, 166

Pacharantanakul, P., & Katz, J. I. 1980, *ApJ*, 238, 985

Pancoast, A., Brewer, B. J., & Treu, T. 2011, *ApJ*, 730, 139

Peterson, B. M. 1993, *PASP*, 105, 247

Peterson, B. M. 2006, *Physics of Active Galactic Nuclei at All Scales*, Springer Lecture Notes in Physics Series, Vol. 693, ed. D. Alloin, R. Johnson, & P. Lira, 77

Pier, E. A., & Krolik, J. H. 1992, *ApJ*, 399, L23

Pier, E. A., & Krolik, J. H. 1993, *ApJ*, 418, 673

Plotkin, R. M. et al. 2010, *ApJ*, 721, 562

Proga, D. 2005, *ApJ*, 630, L9

Pounds, K. & King, A. 2013, *MNRAS*, 433, 1369

Rees, M. J. 1984, *ARA&A*, 22, 471

Sadowski, A., Narayan, R., McKinney, J. C., & Tchekhovskoy, A. 2014, *MNRAS*, 439, 503

Schmitt, H. R., Donley, J. L., Antonucci, R. R. J., et al. 2003, *ApJ*, 597, 768

Shakura, N. I., & Sunyaev, R. 1973, *A&A*, 24, 337

Shemmer, O., Brandt, W. N., Netzer, H., Maiolino, R., & Kaspi, S. 2008, *ApJ*, 682, 81

Shen, Y., & Ho, L. C. 2014, *Nature*, 513, 210

Shull, J. M., Stevans, M., & Danforth, C. W. 2012, *ApJ*, 752, 162

Sticke, J. T., Morris, S. L., Weymann, R. J. & Foltz, C. B. 1992, *ApJ*, 396, 487

Suganuma, M., Yoshii, Y., Kobayashi, Y., et al. 2006, *ApJ*, 639, 46

Svensson, R. & Zdziarski, A. 1994, *ApJ*, 436, 599

Szuszkiewicz, E., Malkan, M. A., & Abramowicz, M. A. 1996, *ApJ*, 458, 474

Telfer, R., Zheng, W., Kriss, G. A. & Davidsen, A. F. 2002, *ApJ*, 565, 773

Vanden Berk, D. E., Richards, G. T., Bauer, A., et al. 2001, *AJ*, 122, 549

Uzdenksy, D. A. 2013, *ApJ*, 775, 103

Wandel, A., Peterson, B. M., & Malkan, M. A. 1999, *ApJ*, 526, 579

Wang, J.-M., Du, P., Baldwin, J. A., et al. 2012, *ApJ*, 746, 137

Wang, J.-M., Du, P., Hu, C., et al. 2014, *ApJ*, 793, 108

Wang, J.-M., Du, P., Valls-Gabaud, D., Hu, C., & Netzer, H. 2013, *Phy. Rev. Lett.*, 110, 081301

Wang, J.-M., & Netzer, H. 2003, *A&A*, 398, 327

Wang, J.-M., Szuszkiewicz, E., Lu, F.-J., & Zhou, Y.-Y. 1999, *ApJ*, 522, 839

Wang, J.-M., Watarai, K.-Y., & Mineshige, S. 2004, *ApJ*, 607, L107

Wang, J.-M., & Zhou, Y.-Y. 1999, *ApJ*, 516, 420

Watarai, K.-Y., Ohsuga, K., Takahashi, R., & Fukue, J. 2005, *PASJ*, 57, 513

Woltjer, L. 1959, *ApJ*, 130, 38

Wu, J., Brandt, W. N., Anderson, S. F., et al. 2012, *ApJ*, 747, 10

Wu, J., Brandt, W. N., Hall, P. B., et al. 2011, *ApJ*, 736, 28

Yang, F., Hu, C., Chen, Y.-M., & Wang, J.-M. 2007, *ChIA&A*, 7, 353

Yang, X.-H., Yuan, F., Ohsuga, K., & Bu, D.-F. 2014, *ApJ*, 780, 79

Zakamska, N. L., & Greene, J. E. 2014, *MNRAS*, 442, 784

Zheng, W., Kriss, G. A., Telfer, R. C., Grimes, J. P., & Davidsen, A. F. 1997, *ApJ*, 475, 469

Zhou, H.-Y., Wang, T.-G., Yuan, W., et al. 2006, *ApJS*, 166, 128

APPENDIX
METHOD TO CALCULATE OCCULTATION

We use the cylindrical coordinate system shown in Figure 3. After some algebraic manipulations, we can show that for a cloud in the BLR located at $P(r_0, \pi/2, z_0)$, the unity vector of the surface at any point on the disk, the direction of the line PQ , and the direction of the cloud are

$$\vec{n} = \frac{1}{\sqrt{1+H_r^2}} (-H_r \cos \phi, -H_r \sin \phi, 1), \quad (\text{A1})$$

$$\vec{n}_1 = \left(\frac{1}{d} \right) (-r \cos \phi, r_0 - r \sin \phi, z_0 - z), \quad (\text{A2})$$

and

$$\vec{n}_0 = \frac{1}{\sqrt{r_0^2 + z_0^2}} (0, r_0, z_0), \quad (\text{A3})$$

respectively, where $d = \sqrt{r^2 - 2rr_0 \sin \phi + r_0^2 + (z_0 - z)^2}$.

Since the disk obscures itself, we neglect the emission from the lower half of the plane and from most of the inner part of the disk through the space around the region between the last stable radius and the Schwarzschild radius. In the Newtonian approximation of a slim disk, general relativistic bending of the photon trajectory can be neglected.

For a cloud located at $(r_0, \pi/2, z_0)$, we first get the tangent line from the cloud to the surface, which satisfies $\vec{n} \cdot \vec{n}_1 = 0$:

$$(r - r_0 \sin \phi) H_r + z_0 - H = 0. \quad (\text{A4})$$

Here H is a function of r . We have a curve (r_t, ϕ_t, H_t) , where the subscript “t” is the tangent point. Extending the tangent line until the intersection R , we have the coordinates of R at (r_c, ϕ_c, H_c) with the disk surface. The points (r_t, ϕ_t, H_t) and (r_c, ϕ_c, H_c) consist of a closed curve $[r_s(\phi)]$ as the boundary between the obscured and unobscured regions. The intersection radius r_c can be between r_{in} and r_{Sch} ; in such a case, we set $r_c = r_{\text{in}}$. The flux received by the cloud is given by

$$F_\nu(r_0, z_0) = \int_0^{2\pi} d\phi \int_{r_s(\phi)}^{\infty} I_\nu(r, \phi, z) (\vec{n} \cdot \vec{n}_1) (\vec{n}_1 \cdot \vec{n}_0) \frac{d\mathcal{S}}{d_0^2}, \quad (\text{A5})$$

where

$$d_0 = [r^2 \cos^2 \varphi + (r \sin \varphi - r_0)^2 + (z - z_0)^2]^{1/2}, \quad (\text{A6})$$

is the distance of the cloud to the center.